

## **Automated Glaucoma Detection Using Hybrid Feature Extraction in Retinal Fundus Images**

RAMA KRISHNAN M, Muthu and FAUST, Oliver

Available from Sheffield Hallam University Research Archive (SHURA) at:

<https://shura.shu.ac.uk/11444/>

---

This document is the Accepted Version [AM]

### **Citation:**

RAMA KRISHNAN M, Muthu and FAUST, Oliver (2012). Automated Glaucoma Detection Using Hybrid Feature Extraction in Retinal Fundus Images. Journal of Mechanics in Medicine and Biology, 13 (1), 1350011-1350032. [Article]

---

### **Copyright and re-use policy**

See <http://shura.shu.ac.uk/information.html>

Journal of Mechanics in Medicine and Biology  
 © World Scientific Publishing Company

## Automated Glaucoma Detection Using Hybrid Feature Extraction in Retinal Fundus Images

Muthu Rama Krishnan M

*Department of Electronics and Computer Engineering, Ngee Ann Polytechnic, Singapore 599489  
 mrk2k2@gmail.com*

Oliver Faust

*School of Electronic Information Engineering, Tianjing University  
 fol2@np.edu.sg*

Received (Day Month Year)

Accepted (Day Month Year)

Glaucoma is one of the most common causes of blindness. Robust mass screening may help to extend the symptom-free life for affected patients. To realize mass screening requires a cost effective glaucoma detection method which integrates well with digital medical and administrative processes. To address these requirements, we propose a novel low cost automated glaucoma diagnosis system based on hybrid feature extraction from digital fundus images. The paper discusses a system for the automated identification of normal and glaucoma classes using Higher Order Spectra (HOS), Trace Transform (TT) and Discrete Wavelet Transform (DWT) features. The extracted features are fed to a Support Vector Machine (SVM) classifier with linear, polynomial order 1, 2, 3 and Radial Basis Function (RBF) in order to select the best kernel for automated decision making. In this work, the SVM classifier, with a polynomial order 2 kernel function, was able to identify glaucoma and normal images with an accuracy of 91.67%, sensitivity and specificity of 90% and 93.33% respectively. Furthermore, we propose a novel integrated index called Glaucoma Risk Index (*GRI*) which is composed from HOS, TT and DWT features, to diagnose the unknown class using a single feature. We hope that this *GRI* will aid clinicians to make a faster glaucoma diagnosis during mass screening of normal/glaucoma images.

keywords Glaucoma; Retina imaging; Computer aided diagnosis; Higher order spectra; Trace transform, Texture; Wavelet; Support vector machine.

1991 Mathematics Subject Classification: 22E46, 53C35, 57S20

### 1. Introduction

Glaucoma is one of the most common causes of blindness. The disease has a mean prevalence of 2.4% for all ages and 4.7% for those aged 75 and above <sup>1</sup>. It is estimated that more than 4 million Americans suffer from glaucoma, and half of them are unaware that they have the disease. Approximately 120000 Americans are blind as a result of glaucoma, thus it is responsible for 9%–12% of all cases of blindness in the U.S <sup>2</sup>. Much of this suffering is preventable, because preventive medicine and

surgical treatment, such as mean trabeculectomy, laser surgery, drainage implants, is available. Unfortunately, glaucoma symptoms are painless and the brain compensates gradual vision impairment to considerable extent. Therefore, early diagnosis is so important to stop or slow down disease progression. However, due to the high mean prevalence of glaucoma, a significant reduction of end stage glaucoma and blindness requires mass screening <sup>3</sup>.

Glaucoma leads to (i) structural changes of the Optic Nerve Head (ONH) and the nerve fibre layer and (ii) simultaneous functional failure of the visual field. The disease is diagnosed based on Intraocular Pressure (IOP), visual field loss tests <sup>4,5</sup> and the manual assessment of the ONH via ophthalmoscopy <sup>3</sup> or stereo fundus imaging <sup>6</sup>. Various algorithms have been used to identify typical features such as abnormality of blood vessels <sup>7</sup> and ONH <sup>8,9</sup>, location and quantification of microaneurisms or drusen <sup>10,11,12</sup>. State of the art glaucoma diagnosis is based on Heidelberg Retinal Tomography (HRT) images. Swindale et al. and Adler et al. have modeled a smooth two-dimensional surface that fitted to the ONH of topography images <sup>13,14</sup>. Damages in the glaucomatous eye were detected using optic disc measures (cup and disc area, height variation using HRT images) <sup>15</sup>. This global shape approach was compared with a sector-based analysis by Lester et al. <sup>16</sup>. Zangwill et al. have automatically diagnosed glaucoma using optic disc parameters, additional parapapillary parameters and Support Vector Machine (SVM) classifier <sup>17</sup>. Most of these shape approaches assumed a valid segmentation of the optic disc. However, a small error in these segmentation based techniques may result in significant changes in the measurements and errors in the diagnosis. Furthermore, HRT imaging is an expensive measurement, because both manpower and equipment cost are high. Now, state of the art glaucoma detection requires mass screening. Hence, the number of measurements is potentially very high and a small cost reduction per measurement will make a large difference.

We attempt to achieve such a small cost reduction by proposing a glaucoma diagnosis system based hybrid feature extraction from digital fundus images. The cost reduction comes from the fact that digital fundus images are less expensive when compared to HRT and the feature extraction is done with inexpensive general purpose computing machines. Furthermore, both processes, image taking and feature extraction, happen in the digital domain, therefore the proposed glaucoma diagnosis system can be easily incorporated into existing medical and administrative workflows. These advantages do not constrain the reliability of the diagnosis support system. To be specific, we show that the proposed system is able to differentiate fundus images from glaucoma patients from those of a normal control group with an accuracy of 91.67%. Furthermore, we propose a novel integrated index, called Glaucoma Risk Index (*GRI*), which is made up of Higher Order Spectra (HOS), Trace Transform (TT) and Discrete Wavelet Transform (DWT) features, to diagnose the unknown class using a single feature.

The layout of the paper is as follows. Section 2 explains the materials and meth-

ods used for this study. Section 3 of the paper presents the hybrid feature extraction methods. Section 4 of the paper presents the SVM classification. The Glaucoma Risk Index is explained in Section 5. The results of the proposed method presents in Section 6. The results are discussed in Section 7 and finally, the paper concludes in Section 8.

## 2. Materials and methods

Figure 1 shows a block diagram of the proposed system. During the pre-processing stage, colored images are converted to grayscale images and the image contrast is increased with histogram equalization. The radon transformation converts 2D images into 1D signals. After these preprocessing steps, important features namely, phase entropy, bispectrum entropy using HOS, triple feature using TT, and average energy of wavelet coefficients are extracted from the image.

The statistical significance of these features is evaluated with the independent sample *t*-test. To evaluate the discriminative powers of these features in a practical setting, they were fed to a SVM classifiers for automated diagnosis support.

### 2.1. Retinal fundus image acquisition

The digital retinal images were collected from the Kasturba Medical College, Manipal, India. We have used 60 fundus images: 30 normal and 30 open-angle glaucoma images from male and female participants which were between 20 and 70 years old. The doctors in the hospitals Ophthalmology Department certified both image quality and usability. The ethics committee, consisting of senior doctors, approved the images for this research. All images were taken with a resolution of  $560 \times 720$  pixels and stored in the uncompressed bitmap format. [Figure 2 shows representative normal and glaucoma sample images to highlight texture variations between the two groups \(column-\(a\): Normal; column-\(b\): Glaucoma\).](#)

### 2.2. Pre-processing

Pre-processing involves two major steps: (i) histogram equalization, and (ii) Radon transformation.

#### 2.2.1. Histogram Equalization

Enhancing the fundus image contrast will aid the feature extraction process. [In this work, colored \(RGB\) eye images are converted to gray scale image by forming a weighted sum of the R, G, and B components using Equation 1.](#)

$$I_{gray} = 0.2989 \times R + 0.5870 \times G + 0.1140 \times B \quad (1)$$

Then the contrast is improved by increasing the dynamic range of the image histogram<sup>18</sup>. This technique assigns pixel intensity values from an input image

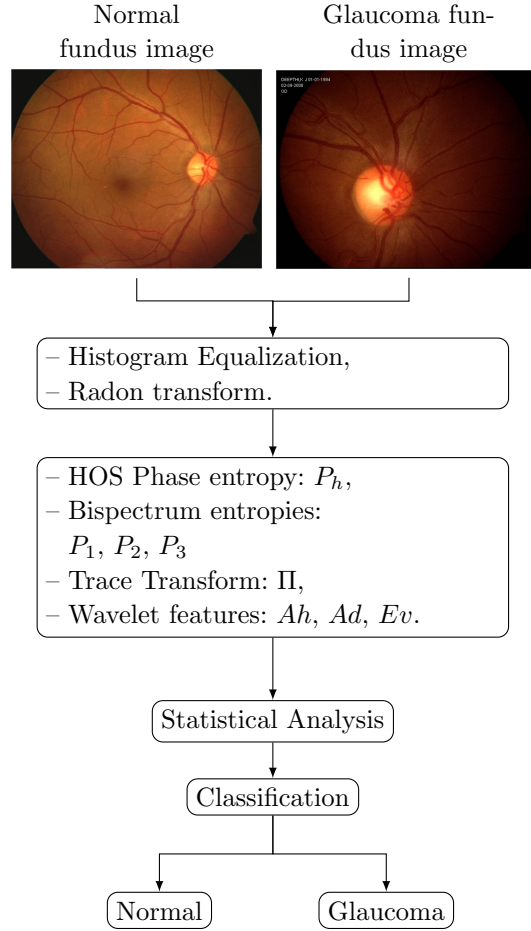


Fig. 1. Block diagram of the proposed automated glaucoma detection system

such that the output image contains a uniform distribution of intensities. As a result, the image contrast is increased. We have used image with good contrast to model a histogram (Figure 3a). This modelled histogram (Figure 3c) is considered as standard and given as an input to the histogram equalization procedure. Finally we have obtained histogram equalized image (Figure 3g).

#### 2.2.2. Radon transform

TT methods, such as the Radon transform, yield many useful features with minimal computational requirements<sup>19</sup>. These features may be devoid of any physical meaning according to human perception, but they can have the right Mathematical properties which distinguish objects.

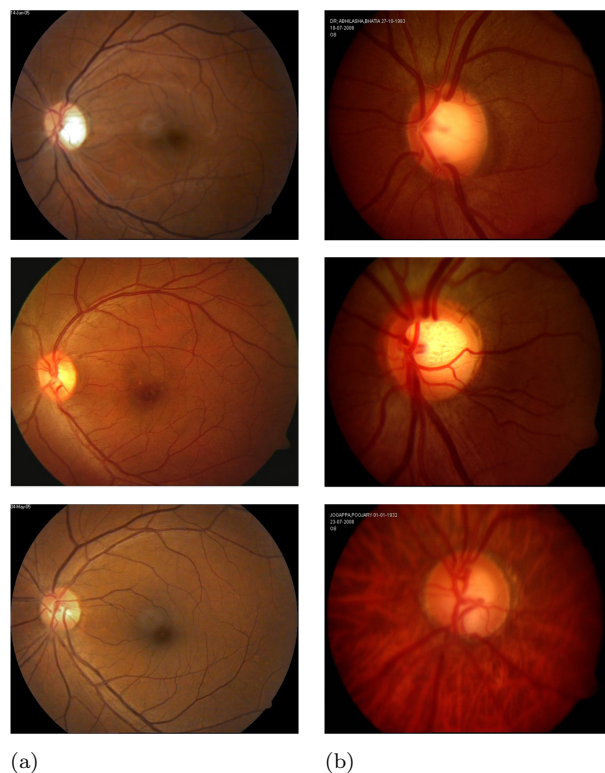


Fig. 2. Representative images: Column-(a): Normal; Column-(b): Glaucoma

The Radon transform is widely used in computed tomography to create an image from scattering data which is associated with cross-sectional scans of an object. It transforms two dimensional images with lines into a domain of possible line parameters, where each line in the image will give a peak positioned to reflect the corresponding line parameters<sup>20</sup>. Hence, lines in the original image are transformed into the points in the Radon domain. The glaucoma image (Figure 3g) is subjected to radon transform with angles varying from  $0^\circ - 180^\circ$  (with  $5^\circ$  interval). Figure 4 shows the results of the Radon transform for  $30^\circ$ ,  $90^\circ$  and  $150^\circ$ .

### 3. Feature Extraction

Texture is an important and widely used feature for analyzing medical images<sup>21,22,23</sup>. In ultrasound medical images<sup>4,24,25</sup> peripapillary chorioretinal atrophy is considered as one of the glaucoma risk factors. It can be identified as bright regions in retinal fundus images, and therefore, incorrectly included as the part of the optic disc regions during the automated disc detection scheme.

6 *Muthu Rama Krishnan M and Oliver Faust*

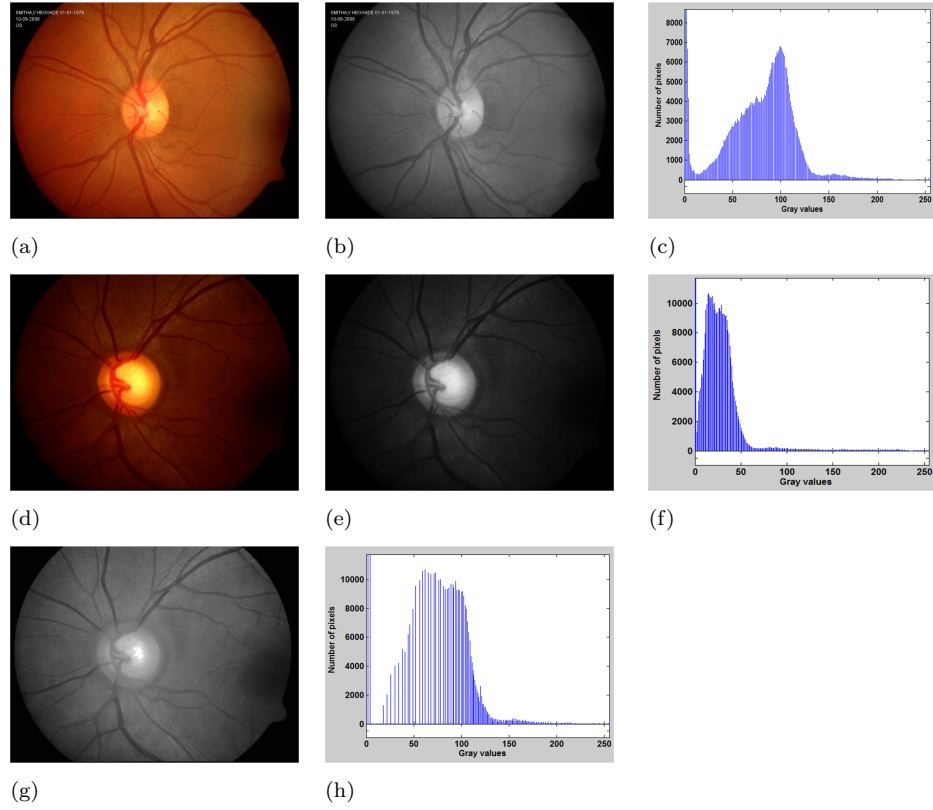


Fig. 3. (a) Standard reference image for histogram equalization; (b) Gray scale image of (a); (c) Histogram of image (b); (d) Original glaucoma image; (e) Gray scale image of (d); (f) Histogram of image (e); (g) Histogram equalized image of (e); (h) Histogram of image (g)

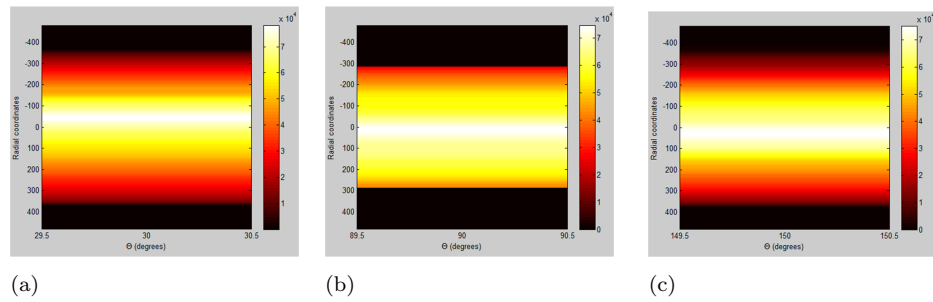


Fig. 4. (a) Radon transform image with angle 30°; (b) Radon transform image with angle 90°; (c) Radon transform image with angle 150°

### 3.1. Higher Order Spectra based features

HOS techniques were first applied to signal processing problems in 1970, subsequently they were used in economics, speech, seismic data processing, plasma physics, optics and biomedical applications<sup>20,26</sup>. Recent studies show that HOS can be used to diagnose epilepsy using Electroencephalography (EEG) signals and cardiac abnormalities using heart rate signals<sup>27,28</sup>. HOS invariants have been used for shape recognition<sup>29</sup> and to identify different kinds of eye diseases<sup>20,4</sup>.

HOS is a nonlinear method which captures subtle changes in image pixels. The algorithm discussion starts with second order statistics which evaluate both mean value ( $m$ ) and variance ( $\sigma^2$ ). They are defined by expectation operation as follows: “ $a$ ” is the result of a random process.

$$\begin{aligned} m_a &= \mathbb{E}\{A\} \\ \sigma_A^2 &= \mathbb{E}\{(A - m_a)^2\} \end{aligned} \quad (2)$$

If  $a$  is a time discrete signal, the second order moment autocorrelation function is defined as:

$$m_a^2(i) = \mathbb{E}\{(A(n) \times A(n+1))\} \quad (3)$$

In addition to these moments, HOS provides higher order moments, i.e.  $m_3$ ,  $m_4$ , ... and nonlinear combinations of the higher order moments called *cumulants*, i.e.  $c_1$ ,  $c_2$ ,  $c_3$ , ... Thus, HOS consists of both moment and cumulant spectra<sup>27,28</sup>. The technique can be used for deterministic and random signals. The so called *bispectrum*, which is a third order statistic, was used in this work. It is obtained by calculating the Fourier transform of the third order correlation of the data:

$$B(f_1, f_2) = \mathbb{E}\{A(f_1) A(f_2) A^*(f_1 + f_2)\} \quad (4)$$

where  $A(f)$  is the Fourier transform of the signal  $a(nT)$  and  $\mathbb{E}\{\cdot\}$  is an average over an ensemble of random signal realizations. For deterministic signals, the relationship holds without an expectation operation. In this case, the third order correlation is a time-average. For deterministic sampled signals,  $A(f)$  is the discrete-time Fourier transform, which, in practice, is computed using the Fast Fourier Transform (FFT) algorithm. The frequency ( $f$ ) may be normalized by the Nyquist frequency to be between 0 and 1 (Figure 5).

In this work, we derived the bispectral phase entropy ( $P_h$ ), entropy 1 ( $P_1$ ), entropy 2 ( $P_2$ ) and entropy 3 ( $P_3$ ). These entropies are similar to the spectral entropy<sup>27,28</sup>. The equations, which govern the phase entropy extraction from HOS parameters, are given below<sup>20</sup>:

$$P_h = \sum_{\langle n \rangle} p(\Psi_n) \log(p(\Psi_n)) \quad (5)$$

$$p(\Psi_n) = \frac{1}{L} \sum_{\langle \Omega \rangle} l(\Phi(B(f_1 f_2)) \in \Psi_n) \quad (6)$$



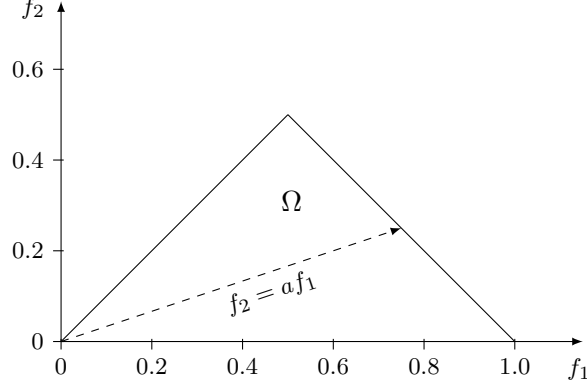


Fig. 5. Non-redundant region of computation of the bispectrum for real signals. Features are calculated by integrating the bispectrum along the dashed line with slope =  $a$ . Frequencies are shown normalized by the Nyquist frequency

$$\Psi_n = \{\Phi | -\pi + 2\pi n/N \leq \Phi < -\pi + 2\pi(n+1)/N\} \quad \text{with } n = 0, 1, \dots, N-1 \quad (7)$$

where  $B$  indicates the bispectrum of the signal,  $L$  is the number of points within the region  $\Omega$ ,  $\Phi$  is the phase angle of the bispectrum, and  $l(\cdot)$  is an indicator function which gives a value of 1 when the phase angle is within the range of  $\Psi_n$ , as depicted by in Equation 6. The three bispectrum entropies are defined as:

$$P_1 = - \sum_{\langle k \rangle} p_k \log(p_k) \quad (8)$$

$$\text{where } p_k = \frac{|B(f_1, f_2)|}{\sum_{\langle \Omega \rangle} |B(f_1, f_2)|}.$$

$$P_2 = - \sum_{\langle i \rangle} p_i \log(p_i) \quad (9)$$

$$\text{where } p_i = \frac{|B(f_1, f_2)|^2}{\sum_{\langle \Omega \rangle} |B(f_1, f_2)|^2}.$$

$$P_3 = - \sum_{\langle n \rangle} p_n \log(p_n) \quad (10)$$

$$\text{where } p_n = \frac{|B(f_1, f_2)|^3}{\sum_{\langle \Omega \rangle} |B(f_1, f_2)|^3}.$$

In this work, we have extracted the four bispectrum invariants, described above, for each radon-transformed fundus image.

### 3.2. Trace Transform (TT)

TT is a generalized approach to the Radon transform, and consists of tracing an image with straight lines along which certain functionals of the so called *image function*. The purpose of a functional is to characterize a function by a number.

Different functionals are used to represent rotation, translation and scaling invariant features of an image. In many cases these features correlate well with the visual textures<sup>19</sup>.

The TT can then be defined as a function  $g$  based on  $\Delta$  with the help of  $T$ , which is some functional of the image function with variable  $t$ .  $T$  is called the trace functional. In order to define a triple feature, two more functionals have been defined and they are designated by  $P$  and  $\Phi$ <sup>19</sup>.  $P$  is known as the diametrical functional, which is a functional of the TT function when it is considered as a function of the length of the normal to the line only.  $\Phi$ , called the *circus functional*, is a functional operating on the orientation variable, after the previous two operations ( $T$  and  $P$ ) have been performed. Thus, the triple feature can be defined as:

$$\Pi = (F, C_1) = \Phi(P(T(F(C_1, \Phi, p, t)))) \quad (11)$$

where  $F(C_1, \Phi, p, t)$  indicates the values of the image function along the chosen line.  $C_1$  is the coordinate system which is parameterized by  $(\Phi, p, t)$ . We calculate two triple features using the invariant functionals. They are as follows:

$$\begin{aligned} \Pi_1 &= T \rightarrow IF_1, P \rightarrow IF_2, \Phi \rightarrow IF_3 \\ \Pi_2 &= T \rightarrow IF_3, P \rightarrow IF_2, \Phi \rightarrow IF_1 \end{aligned} \quad (12)$$

where  $\Pi_1$  is the normalized version of the triple feature formed by using  $IF_1$ ,  $IF_2$  and  $IF_3$  as functionals  $T$ ,  $P$ , and  $\Phi$  respectively in Equation 11.  $\Pi_2$  is the normalized version of the triple feature formed by  $IF_3$ ,  $IF_2$ , and  $IF_1$  as functionals  $T$ ,  $P$ , and  $\Phi$  respectively in Equation 11.  $\Pi_1$  and  $\Pi_2$  are the rotation, scale and translation invariant texture features that are used to quantify a visual texture measure in our application.

### 3.3. Discrete Wavelet Transform Energy Features

Wavelets are mathematical functions that decompose data into different frequency components and subsequently study each component with a resolution which is matched to its scale. The Fourier transform decomposes a signal into a spectrum of frequencies whereas the wavelet analysis decomposes a signal into a hierarchy of scales starting from the coarsest scale<sup>30</sup>. This ability to represent an image at various resolutions makes the Wavelet transform a better tool for extracting features from images than the Fourier transform<sup>31,32</sup>. Multiresolution analysis can be done using Continuous Wavelet Transforms (CWT) and DWT. In our work, we have used DWT for feature extraction, which is explained below.

The DWT transform of a 2D signal  $x(n)$  is evaluated by sending it through a sequence of down-sampling high and low pass filters<sup>33</sup>. The low pass filter is defined by the transfer function  $L(n)$  and the high pass filter is defined by the transfer function  $H(n)$ . The output of the high pass filter  $D(n)$  is known as the detailed

coefficients. The following equation shows how these coefficients are obtained:

$$D(n) = \sum_{k=-\infty}^{\infty} x(k) H(2n - k) \quad (13)$$

The low pass filter output is known as the approximation coefficients. These coefficients are found by using the following equation:

$$A(n) = \sum_{k=-\infty}^{\infty} x(k) L(2n - k) \quad (14)$$

The frequency resolution is further increased by cascading the two basic filter operations. To be specific, the output of the first level low pass filter is fed into the same low and high pass filter combination. The detailed coefficients are output at each level and they form the level coefficients. In general, each level halves the number of samples and doubles the frequency resolution. Consequently, in the final level, both detailed and approximation coefficients are obtained as level coefficients.

In our work, the digital fundus images are represented as an  $m \times n$  gray scale matrix  $I(i, j)$  where each element of the matrix represents the intensity of one pixel. All non-border pixels  $I(i, j)$ , where  $i \notin \{0, m\}$  and  $j \notin \{0, n\}$ , have eight immediate neighboring pixels. These eight neighbors can be used to traverse through the matrix<sup>34</sup>. However, changing the direction with which the matrix is traversed just inverts the sequence of pixels and the 2D DWT coefficients are the same. For example, the Wavelet Packet (WP) result is the same when the matrix is traversed from left to right as from right to left. Therefore, we are left with four possible directions, which are known as decomposition corresponding to  $0^\circ$  (horizontal,  $Dh$ ),  $90^\circ$  (vertical,  $Dv$ ) and  $45^\circ$  or  $135^\circ$  (diagonal,  $Dd$ ) orientations.

In this work level 1 decomposition was sufficient to obtain significant features. We have evaluated 54 wavelet functions. Each of these wavelet functions has a unique low pass filter transfer function  $L(n)$  and a unique high pass filter transfer function  $H(n)$ <sup>33</sup>. We found that Biorthogonal 3.1 (*bior3.1*) outperforms all other tested wavelet functions. Biorthogonal is the name of a wavelet where the associated wavelet transform is invertible but not necessarily orthogonal. Biorthogonal wavelets allow more degrees of freedom than orthogonal wavelets.

The first level 2D DWT yields four resultant matrices, namely  $Dh_1$ ,  $Dv_1$ ,  $Dd_1$  and  $A_1$ , whose elements are intensity values. The following average and mean value

equations were used to extract features from the resultant DWT matrices:

$$\begin{aligned}
 \text{Average } Dh_1(Ah) &= \frac{1}{N \times M} \sum_{x=\langle N \rangle} \sum_{y=\langle M \rangle} |Dh_1(x, y)| \\
 \text{Average } Dv_1(Av) &= \frac{1}{N \times M} \sum_{x=\langle N \rangle} \sum_{y=\langle M \rangle} |Dv_1(x, y)| \\
 \text{Average } Dd_1(Ad) &= \frac{1}{N \times M} \sum_{x=\langle N \rangle} \sum_{y=\langle M \rangle} |Dd_1(x, y)| \\
 \text{Energy } (Ed) &= \frac{1}{N^2 \times M^2} \sum_{x=\langle N \rangle} \sum_{y=\langle M \rangle} (Dd_1(x, y))^2 \\
 \text{Energy } (Ev) &= \frac{1}{N^2 \times M^2} \sum_{x=\langle N \rangle} \sum_{y=\langle M \rangle} (Dv_1(x, y))^2
 \end{aligned} \tag{15}$$

#### 4. Support vector machine

The number of medical diagnosis systems, which use automated classification, is increasing gradually<sup>35</sup>. The evaluation of patient data and decisions by medical experts are the most important factors in diagnosis. Classification systems can help to minimize possible errors and they can provide examination results in a shorter time and in a more detailed manner. In this study, the diagnostic problem is designed based on fourteen features of retinal fundus images, which may be treated as a two-class pattern classification problem.

The SVM algorithm is based on the idea of margin maximization<sup>35,36,37</sup>. The maximum margin can be found by solving the following optimization problem:

$$\begin{aligned}
 &\min \left\{ \frac{1}{2} w^T w + C \sum_{i=1}^l \xi_i^2 \right\} \\
 &s.t. y_i (w^T x_i + b) \geq 1 - \xi_i, \text{ where } i = 1, \xi \geq 0
 \end{aligned} \tag{16}$$

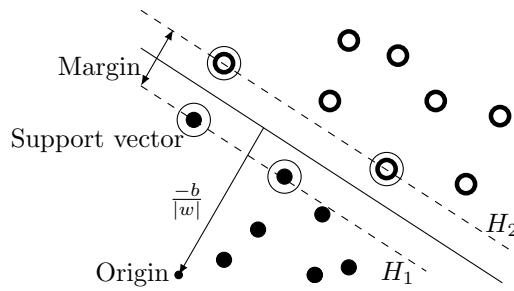


Fig. 6. Optimal separating hyperplanes

The decision function for linear SVMs is given as  $g(x) = w^T x + b$ . In this formulation; we have the training data set  $\{x_i, y_i\}$ ,  $i = 1, \dots, l$ , where  $x_i \in R^n$  are the training data points,  $y_i$  are the class labels,  $l$  is the number of samples and  $n$  is the number of features in each sample. By solving the optimization problem presented

12 *Muthu Rama Krishnan M and Oliver Faust*

in Equation 16, i.e. by finding the parameters  $w$  and  $b$  for a given training set, we are effectively designing a decision hyperplane (Figure 6) over an  $n$  dimensional input space that produces the maximal margin in the space. Generally, the optimization problem, defined in Equation 16, is solved by changing it into the dual problem, as given below:

$$\max \{L_d(\alpha)\} = \sum_{i=1}^l \alpha_i - \frac{1}{2} \sum_{i,j=1}^l y_i y_j \alpha_i \alpha_j x_i^T x_j \quad (17)$$

Subject to  $0 \leq \alpha_i \leq C_i$ , where  $i = 1, \dots, l$ :

$$\sum_{i=1}^l \alpha_i y_i = 0 \quad (18)$$

In this setting, one needs to maximize the dual objective function  $L_d(\alpha)$  with respect to the dual variables  $\alpha_i$  only subject to the box constraints  $0 \leq \alpha_i \leq C$ . The optimization problem can be solved by various established techniques which solve general quadratic programming problems with inequality constraints. The original optimal hyperplane algorithm was a linear classifier. This linear algorithm can be made nonlinear by replacing every dot product by a nonlinear kernel function, such as the Radial Basis Function (RBF).

## 5. Glaucoma Risk Index

We have formulated the *GRI* based on the significant features listed in Table 1. Our approach follows Acharya et al. who have proposed to combine features in such a way that the resulting number or index discriminates normal and disease classes<sup>24</sup>. It is difficult keep track of the individual feature variations. Therefore, we have empirically determined a single integrated index (also called as Glaucoma Risk index) that is a unique combination of the respective features that results in a unique range for both the classes. The utility of such indices is that they can be more comprehensible to the ophthalmologist than the classifiers which are most times black boxes that directly output the class label. Moreover, it is faster and easier to compute and keep track of these indices. When continuously monitored, the variations in the indices can throw light on how the normal become glaucoma over time. In our case, the *GRI* discriminates fundus images which show glaucoma symptoms from normal fundus images.

Equation 19 describes how the features were combined to form the *GRI*.

$$GRI = \frac{\alpha}{\beta \times \gamma} \quad (19)$$

with

$$\begin{aligned}
\alpha &= elres_0 \times epres_{70} \times epres_{75} \times epres_{80} \\
&\quad \times epres_{85} \times epres_{90} \times elres_{90} \\
&\quad \times e2res_{90} \times e3res_{90} \times elres_{180} \\
\beta &= dh1_{\text{norm}} \times dd1_{\text{norm}} \times cvenergy \\
\gamma &= TT_1
\end{aligned} \tag{20}$$

$\alpha$  – indicates the combination of HOS features;  $\beta$  – indicates the combination of wavelet features;  $\gamma$  – indicates the combination of trace transform features.

## 6. Results

In this study, we have used TT, HOS and DWT methods to extract 14 features from digital fundus images. The independent sample  $t$ -test was used to establish the statistical significance of these features. Table 1 shows mean, standard deviation and  $p$ -value of the extracted features. All features, with the exception of  $P_1$ , showed significantly greater values in images taken from glaucomatous participants when compared to the normal control set (Table 1,  $p < 0.01$ ). The low  $p$ -values indicate that all features are extremely useful in differentiating normal images from retinal images with glaucomatous appearance. In the case of HOS-based features, bispectral entropy based features which, were obtained from Radon transform angles  $\Theta = 0^\circ, 70^\circ, 75^\circ, 80^\circ, 85^\circ, 90^\circ, 100^\circ$ , were found to be statistically significant. Among the TT features,  $\Pi_1$  was found to be statistically significant. Finally, the DWT features  $Ad$ ,  $Av$ , and  $Ev$ , based on bior3.1, were found to be statistically significant.

Table 1. Summary of features used in this work

Features	Normal	Glaucoma	$p$ -value
$P_1$ ( $0^\circ$ )	$0.5022 \pm 0.1874$	$0.3834 \pm 0.0851$	0.002502
$P_h$ ( $70^\circ$ )	$1.5415 \pm 0.7583$	$2.2898 \pm 1.0185$	0.002055
$P_h$ ( $75^\circ$ )	$1.5768 \pm 0.7353$	$2.187 \pm 0.778$	0.002797
$P_h$ ( $80^\circ$ )	$1.7648 \pm 0.7481$	$2.3864 \pm 0.7448$	0.002069
$P_h$ ( $85^\circ$ )	$1.9665 \pm 0.6708$	$2.5781 \pm 0.6274$	0.000569
$P_h$ ( $90^\circ$ )	$0.5675 \pm 0.2007$	$0.4495 \pm 0.0607$	0.003134
$P_1$ ( $90^\circ$ )	$0.1222 \pm 0.0768$	$0.0743 \pm 0.0309$	0.00244
$P_2$ ( $90^\circ$ )	$0.0405 \pm 0.0257$	$0.0212 \pm 0.0153$	0.000781
$P_3$ ( $90^\circ$ )	$2.9489 \pm 0.4061$	$3.273 \pm 0.3483$	0.001572
$P_1$ ( $180^\circ$ )	$0.5129 \pm 0.1995$	$0.3757 \pm 0.0801$	0.000912
TT1	$2.6728 \pm 0.5147$	$2.4491 \pm 0.2142$	0.031949
$Ah$	$2.6243 \pm 0.9351$	$1.8899 \pm 0.1584$	8.10E-05
$Ad$	$2.068 \pm 0.7291$	$1.6534 \pm 0.1454$	3.40E-03
$Ev$	$0.0001 \pm 0.0002$	$0.0007 \pm 0.0003$	1.06E-14

Table 2 shows that the  $GRI$  is a highly efficient indicator of the difference between normal and glaucomatous cases. The index can also be employed as an adjunct

tool to cross check the diagnosis of clinicians using just one number. Figure 7 shows the distribution plot of the *GRI* for normal and glaucoma. This plot graphically documents how well this integrated index separates the normal control group from patients with glaucoma.

Table 2. Range of glaucoma risk index for normal and glaucoma dataset

Feature	Normal	Glaucoma	<i>p</i> -value
<i>GRI</i>	$12.41 \pm 0.024$	$1.92 \pm 0.017$	$< 0.0001$

The computation of *GRI* is performed using phase entropy ( $P_h$ ), bispectrum entropies ( $P_1, P_2, P_3$ ) and wavelet energy features ( $Ah, Ad$  and  $Ev$ ). The wavelet energy values of glaucoma are low, this effect may indicate a degeneration of the optic nerve (Table 1), which are expressed as  $\beta$ . The phase entropy values of HOS are high in case of glaucoma, which are expressed as  $\alpha$ . The higher values of HOS features and lower values of wavelet energy features suggest that glaucoma fundus images with glaucoma symptoms have a more coarse textural variation than normal ones. In case of optic nerve hemorrhages, the blood typically collects along the individual nerve fibres that radiate outward from the nerve. Such physiological changes are manifested in fundus images and our experiments show that HOS and DWT features are able to detect and quantify such differences in the eye physiology

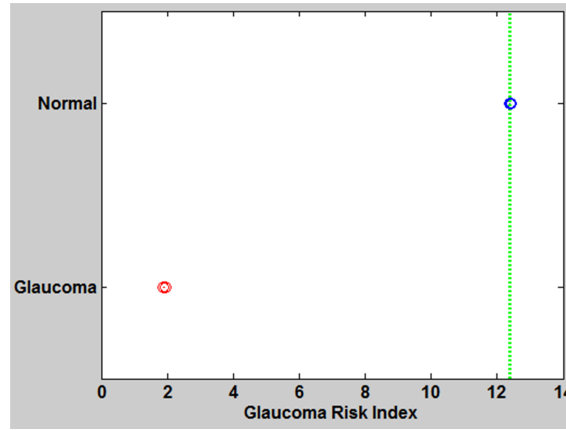


Fig. 7. Plot of GRI for normal and glaucoma classes.

In this work, the so called *three-fold stratified cross validation* method was used to test the classifiers. Two parts of the data (training set) were used for classifier development and one part (test set) is used to test the classifier (i.e. 40 images are

used for training and 20 images were used for testing). This procedure is repeated three times using a different part as the test set in each case. Average of the Accuracy (Acc), Sensitivity (Sn), Specificity (Sp), and Positive Predictive Value (PPV) is calculated for all three trials to obtain the overall performance measures. Table 3 presents the classification results obtained using significant HOS, TT and DWT features from the retinal fundus images. The accuracy registered by SVM with polynomial and linear kernel was 91.67%.

Table 3. Results of SVM classification

SVM kernels	TN	FN	TP	FP	Acc	PPV	Sn	Sp
Linear	10	1	9	0	91.67%	96.67%	86.67%	96.67%
Polynomial degree 2	9	1	9	1	91.67%	93.94%	90%	93.33%
Polynomial degree 3	9	1	9	1	88.33%	88.6%	90%	86.67%
RBF	9	1	9	1	90%	92.96%	86.67%	93.33%

## 7. Discussion

Table 4 presents a summary of the automated glaucoma detection studies which were mentioned in this paper. Many studies have been conducted to develop computer aided decision support systems for the early detection of glaucoma. An Artificial Neural Network (ANN) model, using multifocal visual evoked potential (M-VEP) data, was able to detect glaucoma with a high sensitivity and specificity of 95% and 94%, respectively <sup>38</sup>.

The performance of an ANN, to recognize glaucomatous visual field defects, was studied and its diagnostic accuracy was compared with that of other algorithms which were proposed for the detection of visual field loss <sup>39</sup>. The ANN method showed a sensitivity of 93%, specificity of 94% and an Area under the Receiver Operating Curve (AROC) curve of 0.984. The cluster algorithm achieved a sensitivity of 95% and specificity of 82%.

Nayak et al. have proposed a morphological image processing algorithm based on fundus images to detect glaucoma symptoms. The authors used the cup-to-disc (c/d) ratio, which indicates the distance between the cup portion of the ONH to the diameter of the optic disc, and the ratio of blood vessels area in inferior-superior side to area of blood vessel in the nasal-temporal side considered as features to design a neural network <sup>40</sup>. Their system was able to identify glaucoma with a sensitivity and specificity of 100% and 80%, respectively. A new framework for the detection of glaucoma based on the changes in the ONH, using the method of proper orthogonal decomposition, was proposed <sup>41</sup>. Any glaucomatous changes present in the ONH, during follow-up examinations, were estimated by comparing



follow-up ONH topography with its baseline topograph subspace representation that was constructed earlier. The changes in the ONH were quantified using the following image correspondence measures: L1-norm and L2-norm, correlation, and Image Euclidean Distance (IMED). By using both L2-norm and IMED in the new framework, a AROC of 0.94 was achieved at  $10^\circ$  field of imaging, and 0.91 at  $15^\circ$  field of imaging <sup>41</sup>.

Linear Discriminant Analysis (LDA) and an ANN were used to improve the differentiation between glaucomatous and normal eyes in a Taiwan Chinese population based on the retinal nerve fibre layer thickness measurement data from the Scanning Laser Polarimetry (SLP) with variable corneal compensation <sup>42</sup>. The results showed that the Nerve Fibre Thickness (NFT) parameter produced the highest AROC of 0.932 in differentiating between normal and glaucomatous eyes. The AROCs for the LDA and ANN methods were 0.950 and 0.970, respectively. Hence, the NFT, ANN, and LDF methods demonstrated equal diagnostic power in glaucoma detection.

Principal Component Analysis (PCA) was performed on pixel intensity values. Subsequently, FFT coefficients and spline interpolation data of digital fundus images were used to detect the glaucoma <sup>43</sup>. With an SVM classifier, the investigators obtained an accuracy of 86%.

The Gray Level Co-occurrence Matrix (GLCM) was used for computerized detection of moderate to severe Peripapillary Chorioretinal Atrophy (PPA). Maramatsu et al. obtained a sensitivity and specificity of 73% and 95% respectively <sup>44</sup>.

The gradual loss of the Retinal Nerve Fibres (RNF) is a glaucoma symptom with high diagnostic value. The texture changes in color or grayscale retinal photographs indicate the RNF atrophy <sup>45</sup>. The automated system using fractal and power spectral features coupled with SVM classifier was able to classify the normal and glaucoma groups with an accuracy of 74%.

Nyúl proposed automated glaucoma detection using fundus image features. Initially, variations, such as non-uniform illumination, size differences, and blood vessels were eliminated from the images. Then, PCA was applied in the combined features (Pixel intensities, FFT coefficients and B-Spline coefficients) <sup>3</sup>. These PCA coefficients, combined with a classifier, were able to achieve an accuracy of 80% for detecting glaucomatous retina fundus images.

Acharya et al. <sup>4</sup> proposed a method for glaucoma detection using a combination of texture and HOS features from digital fundus images. Support vector machine, sequential minimal optimization, naive Bayesian, and random-forest classifiers are used to perform supervised classification. The author demonstrated that the texture and HOS features after z-score normalization and feature selection, and when combined with a Random-Forest Classifier (RFC), performs better than the other classifiers and correctly identifies the glaucoma images with an accuracy of more than 91%.

Dua et al. <sup>33</sup> proposed a technique to extract energy signatures obtained using 2-D discrete wavelet transform, and subject these signatures to different feature

ranking and feature selection strategies. The authors gauged the effectiveness of the resultant ranked and selected subsets of features using SVM, sequential minimal optimization, random forest, and naive Bayes classification strategies. The authors obtained an accuracy of around 93% using tenfold cross validations.

Mookiah et al.<sup>5</sup> proposed the system for the automated identification of normal and glaucoma classes using HOS and DWT features. The automated system using HOS and DWT features with SVM classifier was able to identify the glaucoma and normal images automatically with an accuracy of 95%, sensitivity and specificity of 93.33% and 96.67% respectively.

In our present work, we are able to detect the normal and glaucoma classes with accuracy of 91.67%, sensitivity of 90% and specificity of 93.33% using an SVM classifier with polynomial kernel order 2. Furthermore, we show that the *GRI* (Table 3) is a highly effective and accurate tool to differentiate images taken from patients with glaucoma and normal participants. The index can also be employed to assess the efficacy of glaucoma medication.

Table 4. Summary of automated glaucoma detection techniques used in this study.

Authors	Features	Classifier	Performance
Classification using morphological features of the retinal fundus images			
Nagarajan et al. (2002) <sup>38</sup>	Multi focal visual evoked potential	ANN	Sensitivity-95%
Bizios et al. (2007) <sup>39</sup>	ONH parameters	ANN	Sensitivity-93% Specificity-94%
		Cluster algorithm	Sensitivity-95% Specificity-82%
Nayak et al. (2009) <sup>40</sup>	Optic disk parameters Blood vessel parameters	ANN	Sensitivity-100% Specificity-80%
Balasubramanian et al. (2009) <sup>41</sup>	ONH parameters	Proper orthogonal decomposition	AROC-0.94
Huang et al. (2010) <sup>42</sup>	Retinal nerve fibre thickness	LDA	AROC-0.95
		ANN	AROC-0.97
Classification using texture features of the retinal fundus images			
Bock et al. (2007) <sup>43</sup>	PCA, FFT, Spline interpolation data	SVM	Accuracy-86%
Kolar and Jan (2008) <sup>45</sup>	Fractal dimension of RNF	SVM	Accuracy-74%
Nyul (2009) <sup>3</sup>	Pixel intensities, FFT and B-Spline	SVM	Accuracy-80%
Acharya et al. (2011) <sup>4</sup>	Texture and HOS	RFC	Accuracy-91%
Muramatsu et al. (2011) <sup>44</sup>	GLCM features	LDA	Sensitivity-73% Specificity-95%
Dua et al. (2012) <sup>33</sup>	Wavelet	RFC	Accuracy-93%
Mookiah et al. (2012) <sup>5</sup>	HOS and DWT	SVM	Accuracy-95%
<b>This study</b>	HOS, TT, DWT and Energy features	SVM	Sensitivity-90% Specificity-93.33% Accuracy-91.67%

## 8. Conclusion

In this work, we have presented a new automated glaucoma diagnosis system using a combination of HOS, TT and DWT features extracted from digital fundus images. Our system, using SVM classifier (with Polynomial kernel order 2), is able to detect glaucoma and normal classes with an accuracy of 91.67%, sensitivity of 90% and specificity of 93.33%. This classification efficiency may even be further improved using images with a broader range of disease progression, better features and robust data mining algorithms. In addition, we propose an integrated index, which is composed of HOS, TT and DWT features. The *GRI* is a single feature which distinguishes normal and glaucoma fundus images, as shown in Table 3 and Figure 7. Hence, it is a highly effective diagnostic tool which may help clinicians to make faster decisions during mass screening of retinal images.

The proposed system is cost effective, because it integrates seamlessly with digital medical and administrative processes and it incorporates inexpensive general processing components. Therefore, the glaucoma detection system can be used in mass screening where even a modest cost reduction, in the individual diagnosis, amounts to considerable cost savings. Such cost savings help to eliminate suffering, because the money can be used to increase the pervasiveness of glaucoma screening or it can be used anywhere else in the health service where it is even more effective.

## Appendix A. Acronyms

<b>Acc</b>	Accuracy
<b>ANN</b>	Artificial Neural Network
<b>AROC</b>	Area under the Receiver Operating Curve
<b>CWT</b>	Continuous Wavelet Transforms
<b>DWT</b>	Discrete Wavelet Transform
<b>EEG</b>	Electroencephalography
<b>FFT</b>	Fast Fourier Transform
<b>GLCM</b>	Gray Level Co-occurrence Matrix
<b>GRI</b>	Glaucoma Risk Index
<b>HRT</b>	Heidelberg Retina Tomography
<b>HOS</b>	Higher Order Spectra
<b>HRT</b>	Heidelberg Retinal Tomography
<b>IMED</b>	Image Euclidean Distance
<b>IOP</b>	Intraocular Pressure
<b>LDA</b>	Linear Discriminant Analysis
<b>NFT</b>	Nerve Fibre Thickness
<b>ONH</b>	Optic Nerve Head
<b>PCA</b>	Principal Component Analysis
<b>PPA</b>	Peripapillary Chorioretinal Atrophy
<b>PPV</b>	Positive Predictive Value

<b>RBF</b>	Radial Basis Function
<b>RFC</b>	Random-Forest Classifier
<b>RNF</b>	Retinal Nerve Fibres
<b>SLP</b>	Scanning Laser Polarimetry
<b>Sn</b>	Sensitivity
<b>Sp</b>	Specificity
<b>SVM</b>	Support Vector Machine
<b>TT</b>	Trace Transform
<b>WP</b>	Wavelet Packet

## Appendix B. Bibliography

### References

1. R. Bock, J. Meier, L. G. Nyúl, J. Hornegger, G. Michelson, Glaucoma risk index: Automated glaucoma detection from color fundus images., *Medical Image Analysis* 14 (2010) 471–481.
2. Glaucoma research foundation,  
Accessed: 01/05/2012.  
URL [http://www.glaucoma.org/learn/glaucoma\\_facts.php](http://www.glaucoma.org/learn/glaucoma_facts.php)
3. L. G. Nyúl, Retinal image analysis for automated glaucoma risk evaluation, in: J. Liu, K. Doi, A. Fenster, S. C. Chan (Eds.), *MIPPR 2009: Medical Imaging, Parallel Processing of Images, and Optimization Techniques*, SPIE, 2009, pp. 1–9.
4. U. R. Acharya, S. Dua, X. Du, S. Vinitha Sree, C. K. Chua, Automated diagnosis of glaucoma using texture and higher order spectra features, *Information Technology in Biomedicine, IEEE Transactions on* 15 (3) (2011) 449–455.
5. M. R. K. Mookiah, U. R. Acharya, C. M. Lim, A. Petznick, J. S. Suri, Data mining technique for automated diagnosis of glaucoma using higher order spectra and wavelet energy features, *Knowledge-Based Systems* 33 (0) (2012) 73–82.
6. S. C. Lin, K. Singh, H. D. Jampel, E. A. Hodapp, S. D. Smith, B. A. Francis, D. K. Dueker, R. D. Fechtner, J. S. Samples, J. S. Schuman, D. S. Minckler, Optic nerve head and retinal nerve fiber layer analysis: A report by the american academy of ophthalmology, *Ophthalmology* 114 (10) (2007) 1937–1949.
7. J. Staal, M. D. Abramoff, M. Niemeijer, M. A. Viergever, B. van Ginneken, Ridge-based vessel segmentation in color images of the retina, *Medical Imaging, IEEE Transactions on* 23 (4) (2004) 501–509.
8. R. Chrastek, M. Wolf, K. Donath, H. Niemann, D. Paulus, T. Hothorn, B. Lausen, R. Lämmer, C. Y. Mardin, G. Michelson, Automated segmentation of the optic nerve head for diagnosis of glaucoma, *Medical Image Analysis* 9 (4) (2005) 297–314.
9. A. Hoover, M. Goldbaum, Locating the optic nerve in a retinal image using the fuzzy convergence of the blood vessels, *Medical Imaging, IEEE Transactions on* 22 (8) (2003) 951–958.
10. T. Walter, J.-C. Klein, Automatic detection of microaneurysms in color fundus images of the human retina by means of the bounding box closing, in: *Proceedings of the Third International Symposium on Medical Data Analysis, ISMDA '02*, Springer-Verlag, London, UK, UK, 2002, pp. 210–220.
11. K. Rapantzikos, M. E. Zervakis, K. Balas, Detection and segmentation of drusen deposits on human retina: Potential in the diagnosis of age-related macular degeneration., *Medical Image Analysis* 7 (1) (2003) 95–108.

12. W. L. Yun, U. R. Acharya, Y. V. Venkatesh, C. Chee, L. C. Min, E. Y. K. Ng, Identification of different stages of diabetic retinopathy using retinal optical images, *Inf. Sci.* 178 (1) (2008) 106–121.
13. N. V. Swindale, G. Stjepanovic, A. Chin, F. S. Mikelberg, Automated analysis of normal and glaucomatous optic nerve head topography images, *Investigative Ophthalmology & Visual Science* 41 (7) (2000) 1730–1742.
14. R. A. Abdel-Ghaffar, T. Morris, T. Ritchings, I. Wood, Detection and characterisation of the optic disk in glaucoma and diabetic retinopathy, *Proceedings MIUA 2004* (2004) 2–5.
15. H. Uchida, L. Brigatti, J. Caprioli, Detection of structural damage from glaucoma with confocal laser image analysis., *Investigative Ophthalmology & Visual Science* 37 (12) (1996) 2393–2401.
16. M. Iester, N. V. Swindale, F. S. Mikelberg, Sector-based analysis of optic nerve head shape parameters and visual field indices in healthy and glaucomatous eyes, *J Glaucoma* 6 (1997) 371–376.
17. L. M. Zangwill, K. Chan, C. Bowd, J. Hao, T.-W. Lee, R. N. Weinreb, T. J. Sejnowski, M. H. Goldbaum, Heidelberg retina tomograph measurements of the optic disc and parapapillary retina for detecting glaucoma analyzed by machine learning classifiers, *Investigative Ophthalmology & Visual Science* 45 (9) (2004) 3144–3151.
18. R. C. Gonzalez, R. E. Woods, *Digital Image Processing*, 2nd Edition, Addison-Wesley Longman Publishing Co., Inc., Boston, MA, USA, 1992.
19. A. Kadyrov, M. Petrou, The trace transform and its applications, *IEEE Trans. Pattern Anal. Mach. Intell.* 23 (8) (2001) 811–828.
20. U. R. Acharya, C. K. Chua, E. Y. Ng, W. Yu, C. Chee, Application of higher order spectra for the identification of diabetes retinopathy stages, *J. Med. Syst.* 32 (6) (2008) 481–488.
21. T. M. A. Basile, L. Caponetti, G. Castellano, G. Sforza, A texture-based image processing approach for the description of human oocyte cytoplasm, *Instrumentation and Measurement*, *IEEE Transactions on* 59 (10) (2010) 2591–2601.
22. N. Szekeley, N. Toth, B. Pataki, A hybrid system for detecting masses in mammographic images, *Instrumentation and Measurement*, *IEEE Transactions on* 55 (3) (2006) 944–952.
23. J.-H. Tan, E. Y. K. Ng, U. R. Acharya, C. Chee, Infrared thermography on ocular surface temperature: A review, *Infrared Physics & Technology* 52 (4) (2009) 97–108.
24. U. R. Acharya, O. Faust, V. S. Sree, F. Molinari, R. Garberoglio, J. S. Suri, Cost-effective and non-invasive automated benign and malignant thyroid lesion classification in 3d contrast-enhanced ultrasound using combination of wavelets and textures: A class of thyroscan(tm) algorithms., *Technol Cancer Res Treat* 10 (4) (2011) 371–80.
25. J. Stoitsis, S. Golemati, K. S. Nikita, A. N. Nicolaides, A modular software system to assist interpretation of medical images application to vascular ultrasound images, in: *Imaging Systems and Techniques*, 2004. (IST). 2004 IEEE International Workshop on, 2004, pp. 135–140.
26. U. R. Acharya, E. C. Chua, K. C. Chua, L. C. Min, T. Tamura, Analysis and automatic identification of sleep stages using higher order spectra, *International Journal of Neural Systems* 20 (6) (2010) 509–521.
27. K. C. Chua, V. Chandran, U. Rajendra Acharya, C. M. Lim, Analysis of epileptic eeg signals using higher order spectra, *Journal of Medical Engineering & Technology* 33 (1) (2009) 42–50.
28. K. C. Chua, V. Chandran, U. R. Acharya, C. M. Lim, Cardiac state diagnosis us-

- ing higher order spectra of heart rate variability, *Journal of Medical Engineering & Technology* 32 (2) (2008) 145–155.
29. V. Chandran, B. Carswell, B. Boashash, S. Elgar, Pattern recognition using invariants defined from higher order spectra: 2-d image inputs, *Image Processing, IEEE Transactions on* 6 (5) (1997) 703–712.
  30. M. Vetterli, C. Herley, Wavelets and filter banks: theory and design, *Signal Processing, IEEE Transactions on* 40 (9) (1992) 2207–2232.
  31. R. Ramesh, M. Madheswaran, K. Kannan, Nanoscale finfet sensor for determining the breast cancer tissues using wavelet coefficients, *Journal of Mechanics in Medicine and Biology* 11 (2011) 1295–1314.
  32. V. S. Chourasia, A. K. Tiwari, R. Gangopadhyay, Time-frequency characterization of fetal phonocardiographic signals using wavelet scalogram, *Journal of Mechanics in Medicine and Biology* 11 (2011) 391–406.
  33. S. Dua, U. R. Acharya, P. Chowriappa, S. V. Sree, Wavelet-based energy features for glaucomatous image classification, *Information Technology in Biomedicine, IEEE Transactions on* 16 (1) (2012) 80–87.
  34. H. Yuan, J. Gao, H. Z. Guo, C. Lu, An efficient method to process the quantized acoustoelectric current: Wavelet transform, *Instrumentation and Measurement, IEEE Transactions on* 60 (3) (2011) 696–702.
  35. J. Ren, Ann vs. svm: Which one performs better in classification of mccs in mammo-gram imaging, *Know.-Based Syst.* 26 (2012) 144–153.
  36. V. N. Vapnik, *The Nature of Statistical Learning Theory*, Statistics for Engineering and Information Science, Springer, 2000.
  37. R. J. Martis, C. Chakraborty, Arrhythmia disease diagnosis using neural network, svm and genetic algorithm optimized k-means clustering, *Journal of Mechanics in Medicine and Biology* 11 (2011) 897–915.
  38. R. Nagarajan, C. Balachandran, D. Gunaratnam, A. Klistorner, S. Graham, Neural network model for early detection of glaucoma using multi-focal visual evoked potential (m-vep), *Invest. Ophthalmol. Vis. Sci.* 43 (12) (2002) 39–52.
  39. D. Bizios, A. Heijl, B. Bengtsson, Trained artificial neural network for glaucoma diagnosis using visual field data: A comparison with conventional algorithms, *Journal of Glaucoma* 16 (2007) 20–28.
  40. J. Nayak, U. R. Acharya, P. S. Bhat, N. Shetty, T.-C. Lim, Automated diagnosis of glaucoma using digital fundus images, *J. Med. Syst.* 33 (5) (2009) 337–346.
  41. M. Balasubramanian, S. Žabic, C. Bowd, H. W. Thompson, P. Wolenski, S. S. Iyengar, B. B. Karki, L. M. Zangwill, A framework for detecting glaucomatous progression in the optic nerve head of an eye using proper orthogonal decomposition, *Trans. Info. Tech. Biomed.* 13 (5) (2009) 781–793.
  42. M.-L. Huang, H.-Y. Chen, W.-C. Huang, Y.-Y. Tsai, Linear discriminant analysis and artificial neural network for glaucoma diagnosis using scanning laser polarimetry-variable cornea compensation measurements in taiwan chinese population, *Graefe's Archive for Clinical and Experimental Ophthalmology* 248 (2010) 435–441.
  43. R. Bock, J. Meier, G. Michelson, L. G. Nyúl, J. Hornegger, Classifying glaucoma with image-based features from fundus photographs, in: *Proceedings of the 29th DAGM conference on Pattern recognition*, Springer-Verlag, Berlin, Heidelberg, 2007, pp. 355–364.
  44. C. Muramatsu, Y. Hatanaka, A. Sawada, T. Yamamoto, H. Fujita, Computerized detection of peripapillary chorioretinal atrophy by texture analysis, in: *Engineering in Medicine and Biology Society, EMBC, 2011 Annual International Conference of the IEEE*, 2011, pp. 5947–5950.

22 *Muthu Rama Krishnan M and Oliver Faust*

45. R. Kolar, J. Jan, Detection of glaucomatous eye via color fundus images using fractal dimensions., Radio engineering 17 (2008) 109–114.